OPTICA

Deep-learning-based colorimetric polarization-angle detection with metasurfaces

Bo Yang,[1,†] **Dina Ma,**[1,†] **Wenwei Liu,**[1,†] **Duk-Yong Choi,**[2] **Zhancheng Li,**[1] **Hua Cheng,**[1,5] **Jianguo Tian,**[1] **and Shuqi Chen**[1,3,4,6]

[1]*The Key Laboratory of Weak Light Nonlinear Photonics, Ministry of Education, Renewable Energy Conversion and Storage Center, School of Physics and TEDA Institute of Applied Physics, Nankai University, Tianjin 300071, China*
[2]*Laser Physics Centre, Research School of Physics, Australian National University, Canberra, ACT 2601, Australia*
[3]*The Collaborative Innovation Center of Extreme Optics, Shanxi University, Taiyuan, Shanxi 030006, China*
[4]*The Collaborative Innovation Center of Light Manipulations and Applications, Shandong Normal University, Jinan 250358, China*
[5]*e-mail: hcheng@nankai.edu.cn*
[6]*e-mail: schen@nankai.edu.cn*

Polarization plays a key role in both optics and photonics. Generally, the polarization states of light are measured with birefringent or dichroic optical elements paired with a power meter. Here we propose a direct polarization detection method based on colorimetric asymmetrical all-dielectric metasurfaces to obtain the polarization angles of the incident light. The independently tunable periods and diameters along the *x* and *y* axes enables double-layer nanopillars to realize high-performance dual-color palettes with arbitrary combinations under orthogonal polarization states. The polarization detection network based on residual networks is used to deeply learn the regulations between color palette variations and incident polarization angles, which can accurately recognize extremely slight polarization variations in about 1 s with an accuracy of 81.4% within 0.7° error and 99.5% within 1.4° error. Our strategy significantly improves the compactness of polarization detection, and it can be readily expanded to polarization distribution measurement and colorimetric polarization imaging on an intelligent platform. © 2022 Optica Publishing Group under the terms of the Optica Open Access Publishing Agreement

Color, the information carrier of our surroundings, has been a powerful diagnostic tool since ancient times. Recently, colorimetric sensing that utilizes output color variations to characterize the input stimuli variations, such as refractive index, temperature, pH, and humidity, has been a practical and low-cost way to realize rapid and visual detection in the fields of biology, biomedicine, and environmentology [1–3]. However, conventional colorimetric sensing relying on special physical or chemical effects (such as particle aggregation and surface wetting) is restricted by low sensibility of color response to weak input stimuli [4,5]. With the advances of nanofabrication technology, metasurfaces as two-dimensional artificial elements have brought about high-performance colorimetric sensors in the past decade [6,7] because the interaction between light and plasmonic or dielectric nanostructures enables high-resolution, high-quality, and high-compactness structural

colors [8–12]. Particularly a weak extrinsic stimulus such as a perturbation in the surrounding environment or the incident light can readily lead to tunable structural colors [6]. For example, the difference of refractive indices between surrounding environment and nanostructures can yield the shifting of plasmonic or Mie resonant peaks in the visible waveband, namely, color variations [13,14]. Fan *et al.* have reported colorimetric ricin sensing based on a nanopin-cavity resonator, exhibiting clear color variation to visualize and recognize the concentration of ricin solutions [13].

On the other hand, the varying polarization angles of incident light enable the asymmetric nanostructures to significantly realize tunable colors [15,16]. By independent design of periods and diameters along *x* and *y* axes, arbitrary combinations of dual colors across the entire visible wavelengths under orthogonal polarization states have been reported recently [16]. High-performance colors can regularly change when the polarization angles vary, providing a promising method for colorimetric polarization-angle detection, which is essential for practical applications in modern optics, such as communications, remote sensing, imaging, biomedical diagnosis, and so on [17,18]. Nevertheless, current colorimetric sensing designs mostly rely on naked eyes to perceive colors variations, which is hard to quantitatively analyze and limits the detection resolution.

In recent years, deep learning has had great success in computer science and has boosted the development of data-driven artificial intelligence technologies such as computer vision [19,20], speech recognition [21], and decision making [22]. Recent works in photonics have demonstrated that deep learning can accurately predict resonance spectra and perform the inverse design of photonic devices [23,24]. It can also be used to optimize classification problems such as superhigh-resolution recognition of orbital angular momentum [25] and accurate phase prediction for anisotropic digital coding metasurfaces [26]. The most popular network used in deep learning is the deep convolutional neural network (CNN), which can be used in applications such as classification tasks [27]. He *et al.* [28] proposed a design of residual networks (ResNets) that can scale up to thousands of layers and still have excellent

performance; these are of great interest in the precise measurement of physical quantities in photonics.

In this Letter, we realize quantitatively colorimetric polarization-angle detection with asymmetrical all-dielectric meta-surfaces by performing a polarization detection network (PDN) based on ResNets. Taking advantage of the high-performance colors resulting from index matching in $SiO_2 - TiO_2$ nanopillars [10], we employ a PDN to analyze the color patterns of an arrayed color palette and accurately recognize the incident polarization variation with measured accuracy reaching 81.4% within 0.7° error and 99.5% within 1.4° error. This work could inspire new directions in polarization detection devices, full-color polarization display, and imaging in metasurface technology.

Figure 1 illustrates the process of colorimetric polarization-angle detection. To obtain polarization-sensitive structural colors, we designed asymmetric nanopillars with high-performance structural colors variation when varying the incident polarization angles ($\varphi_{incident}$). An arrayed color palette with abundant combinations of dual colors is used as input. Plenty of measured inputs under different polarized light were collected by an automatic optical setup, in which 69% of the data were used as the training dataset and 31% of the data were used as test ones. Extremely slight color variations can be recognized based on PDN, leading to colorimetric polarization-angle ($\varphi_{detection}$) detection. Once the network has been trained, the polarization angle can be obtained in about 1 s.

To broaden the gamut of color switching, we designed an all-dielectric metasurface where the TiO_2 and SiO_2 layers with thickness of 200 nm (H_2) and 100 nm (H_1) are successively deposited on SiO_2 substrate as shown in Fig. 2(a). We fabricated the $SiO_2 - TiO_2$ nanopillars by electron beam lithography and plasma etching to verify the highly saturated colors. Figure 2(b) presents the SEM images of the double-layer nanopillars in top and side views. By independently modulating the periods (P_x/P_y) and diameters (D_x/D_y) along the x and y axes, we can realize wide and flexible switching of colors under orthogonal polarization states. The high-monochromaticity reflection spectra with narrow peaks at resonant wavelengths and remarkably low reflection at non-resonant wavelengths can be obtained owing to the index matching between TiO_2 and SiO_2 layers in terms of $\sqrt{n_{TiO_2} \cdot n_{air}} \approx n_{SiO_2}$. The SiO_2 layer serves as an antireflection layer to suppress the excitation of multipolar modes including dipoles and quadrupoles at the non-resonant wavelengths, resulting in high monochromaticity of the reflection spectra [10].
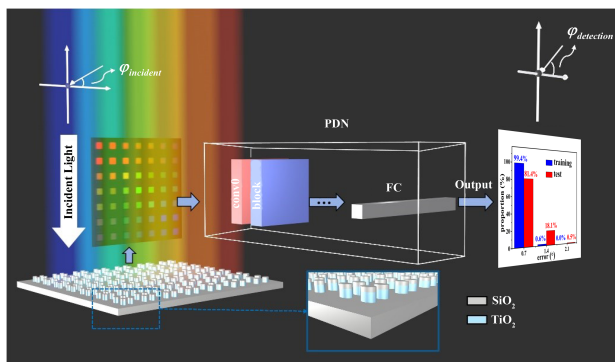
Fig. 1. Schematic of colorimetric polarization-angle detection. The arrayed color palette of $SiO_2 - TiO_2$ metasurfaces changes accordingly with varying $\varphi_{incident}$, which can be detected by deep learning with PDN.

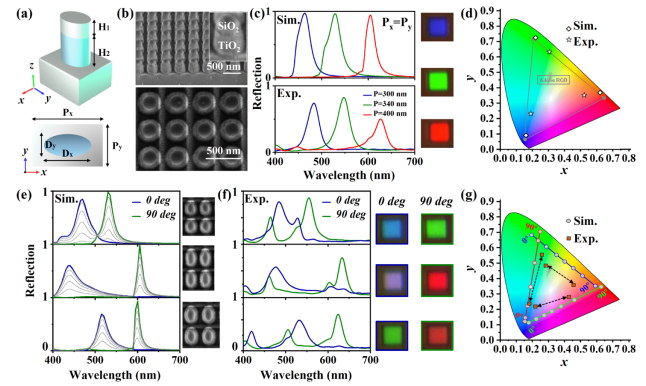**Fig. 2.** Highly saturated polarization-sensitive structural colors based on $SiO_2 - TiO_2$ nanostructures. (a) Schematic of the nanopillar. (b) SEM images of the metasurface in side and top view. (c) Simulated and measured spectra and colors patterns for three-primary-color symmetrical pixels. (d) The three-primary-color pixels in (c) in the 1931 CIE chromaticity diagram. (e) Simulated and (f) measured spectra and measured color patterns for three-primary-color switching pixels with $\varphi_{incident}$ varing from 0° to 90°. The gray lines represent $\varphi_{incident}$ within 0° and 90°. (g) Simulated (circles) and measured (squares) three-primary-color switching.

The simulated and measured spectra are shown in Fig. 2(c) for symmetrical nanostructures ($P_x = P_y$, $D_x = D_y$). Three high-quality primary colors can be realized when the period/diameter is set as 300 nm/170 nm, 340 nm/210 nm, and 400 nm/250 nm. The measurements show high-efficiency and narrow-bandwidth reflection spectra with ultralow efficiency at non-resonant wavelengths. Although the fabricated nanopillars hold a slant cross section on the lateral side due to the different etch resistances of TiO_2 and SiO_2 layers, the measured spectra in Fig. 2(c) match well with the simulated results. The slight redshift and reduced efficiency of the measured spectra result from the fabrication imperfection including etching dose, roughness of surface, and deformation of shapes. The captured patterns of the three-primary-color pixels in Fig. 2(c) also exhibit vivid and highly saturated colors in the experiment, proving that the $SiO_2 - TiO_2$ nanopillars have significant superiority in realizing highly saturated colors with a huge gamut. The corresponding chromaticity coordinates of the simulated and measured results are drawn in the 1931 CIE chromaticity diagram in Fig. 2(d), showing that the $SiO_2 - TiO_2$ nanopillars can realize colors with a wide gamut approaching Adobe RGB space (gray triangle) in simulation.

By meticulously designing the geometrical parameters (P_x, P_y, D_x, D_y), arbitrary combinations of color switching covering a wide gamut can be realized under orthogonal polarization angles. We first design three-primary-color switching pixels (i.e., the switching between blue and green, blue and red, green and red) under x (0°) and y (90°) polarization states with the parameters (P_x, P_y, D_x, D_y) of (280, 340, 170, 230 nm), (270, 400, 160, 290 nm), and (330, 400, 180, 279 nm), respectively. Figure 2(e) shows simulated spectra of the switching pixels when the incident polarization angle varies from 0° to 90°, exhibiting the reflection-peak switching from 440 to 605 nm with high monochromaticity. We measured the reflection spectra and imaged the color patterns with the polarization angles changing from 0° to 90° [Fig. 2(f)]. The deviation between simulated and measured spectra is attributed to the slant cross section of the fabricated nanopillars. The effective refractive index and scattering cross section of the nanopillars will be

decreased with increase of the gap size, resulting in splitting resonant peak. According to Malus's law, the reflection spectra follow a sinusoidal transformation and superposition of different angles $R(\varphi_{incident}, \lambda) = R_x(\lambda)\sin^2\varphi_{incident} + R_y(\lambda)\cos^2\varphi_{incident}$, where $R_x(\lambda)$ and $R_y(\lambda)$ represent the reflection spectra under x and y polarization states. For arbitrary linear polarization angles, the corresponding color is a mixing of the initial colors under x and y polarization states with specific proportion as a function of $\varphi_{incident}$. As the simulated (dots) and measured (squares) chromaticity coordinates show in the 1931 CIE diagram [Fig. 2(g)], switching of colors with ultrahigh saturation can be realized, significantly covering a wide gamut. The polychrome lines with dots in the 1931 CIE diagram show that the structural colors regularly switch when the incident polarization angles change from 0° to 90°. Therefore, the color variations generated from the asymmetrical nanopillars can be used as a medium to characterize the polarization angles of linear incident light, namely, colorimetric polarization-angle detection.

To increase the resolutions of color variations and improve the detection accuracy when the polarization angle changes, we fabricated a color palette with abundant combinations of color switching based on the $SiO_2 - TiO_2$ nanostructures. 7×7 samples with width of 25 μm were fabricated, in which the periods gradually increase from 280 to 400 nm with a 20 nm increment along the x and y axes, respectively. The CCD camera and brushed motor controlling $\varphi_{incident}$ were connected by the software of Labview to automatically capture the color palettes for different polarization states. Three different illuminants including xenon (Xe) illuminant, bromine tungsten (Br-W) illuminant, and D50 illuminant were respectively applied to enrich the dataset in the experiment. The captured images are shown in Fig. 3 when the polarization angles are 0°, 45°, and 90°, indicating vivid and massive color switching under distinct incident polarization states. For instance, when the incident polarization angles vary from 0° to 90°, the color patterns in the white dashed box switch from blue to aquamarine blue, blue to green, and blue to red. We collected an abundant dataset including 1801 (polarization angles varying from 0° to 90° with a 0.05° step) ×3 (three different illuminants) images of color palettes for deep learning.

PDN, whose main structure is consistent with that of Res-34 [28], is employed to quantitatively learn the relations between $\varphi_{incident}$ and color variations. As shown in Fig. 4(a), the designed networ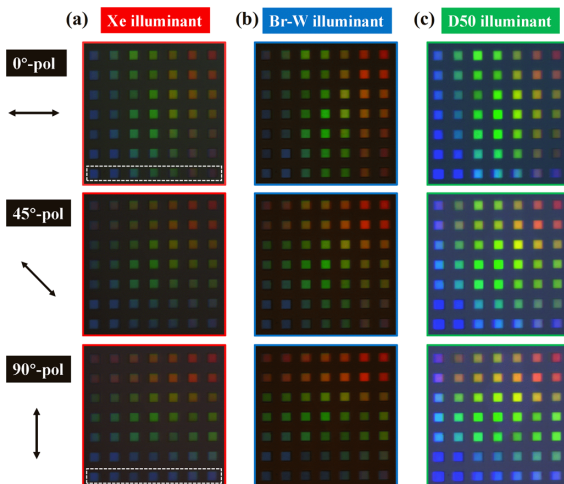k consists of many stacked residual blocks, and the distribution of residual blocks can be summarized as 3×3 Convolution (Conv) - Batch Normalizing transform (BN) - Rectified Linear Unit (ReLU)–3×3 Conv–BN–ReLU. The conv0 layer corresponds to the sequence 7×7 Conv (2 strides)–BN–ReLU. After the conv0 layer and a max pooling (MP) layer with two strides, the input then passes through four blocks. The number of residual blocks of each block are {3, 4, 6, 3}, respectively. Each Conv layer in the kth block can produce $64 \times 2^{k-1}$ feature maps. The feature-map sizes in the four blocks are 28×28, 14×14, 7×7, and 4×4. The PDN ends with a global average pooling (GAP) layer and a 129-way fully connected (FC) layer. We employed a cross-entropy loss function of the form $loss(x, class) = -\log(\frac{\exp(x[class])}{\sum_j \exp(x[j])}) = -x[class] + \log(\sum_j \exp(x[j]))$, where x is the output and class is the true label of the input image. The color palettes are down sampled to 112×112 pixels as input of the PDN. The full dataset contains 1801 polarization angles and is divided into classes at intervals of 0.7°, i.e., $class_j = \lfloor \frac{\varphi_{incident,i}}{0.7} \rfloor$. We use the adaptive moment estimation (Adam) optimizer with the batch size of 124 for 4380 iterations. The initial learning rate is set to be 0.0001, which is lowered by 10 times and 5 times at 1200 and 2700 iterations, respectively. We trained our PDN network on a single Quadro RTX 6000 GPU with a weight decay of 0.00001. The number of images in the training set and the test set are 3720 and 1683, respectively. In each iteration, we randomly selected 124 data from the test dataset to calculate the loss function and prediction accuracy of the test set. The loss function values of the training dataset and test dataset in Fig. 4(b) indicate that the loss can be reduced to 0.5 after 4380 iterations. After training, we input the test dataset separately into PDN for evaluating the classification performance. Taking classes from 91 to 98 as an example, the confused matrix in Fig. 4(c) shows the predicted polarization angles of the test dataset, which consists of 12, 13, 12, 14, 14, 13, 16, and 14 images to be tested. It can be seen that a large proportion of tested polarization angles are correctly recognized. Other color bases, such as Cyan-Magenta-Yellow (CMY) or even the mixture of RGB and CMY, can also realize polarization detection by delicately adjusting the nanostructure designs with anisotropic color responses. The errors are caused mainly by the classification boundary, such as 0.69° and 0.7°. Although the two angles are very close, they belong to different categories, leading to an increased
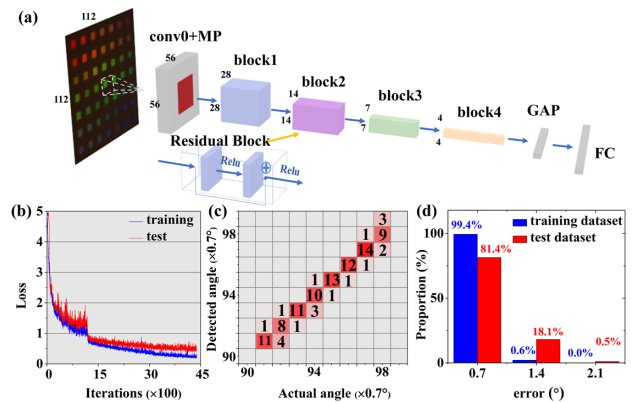

Fig. 3. Measured color palettes of arrayed samples with varying periods (P_x, P_y) and diameter (D_x, D_y) under (a) Xe, (b) Br-W, and (c) D50 illuminant with $\varphi_{incident}$ of 0°, 45°, and 90°.

Fig. 4. (a) Sketch map of PDN to learn the relations between color variations of palettes and $\varphi_{incident}$. (b) The loss curves of training dataset (blue line) and test dataset (red line) as a function of iterations. (c) Confusion matrix from 91 (63.7°) to 98 classes (68.6°) of the test dataset. (d) The proportions for the training dataset and test dataset for different detection errors.

error. As a result, it predicts the polarization angles with an accuracy of 99.4% within 0.7° error (100% within 1.4°) for the training dataset and 81.4% within 0.7° error (99.5% within 1.4° error) for the test dataset [Fig. 4(d)]. The percentage of the training dataset is chosen to be 69% to keep the error of the test dataset in the range of 0° to 2.1°. The polarization detection accuracy is decided by the RGB sensitivity to the polarization angle. The larger the RGB gradient for polarization angle, the greater the detection accuracy. The absolute polarization-angle detection can also be achieved in our scheme. The corresponding accuracy is decided by the amount of datasets and the calibration precision in the experiments, i.e., the accuracy of the electric rotary stage 0.05°. Our method can be implemented under a fixed incident angle range to eliminate the spectra uncertainty originating from different incident angles. We used an objective (NA = 0.3 corresponding the incident angle from 0 to 17.5°) to illuminate and collect light, which guarantees a lack of obvious fluctuations for the bright colors.

In conclusion, we propose quantitatively a colorimetric polarization-angle detection method empowered by PDN based on asymmetrical all-dielectric metasurfaces. The index matching in $SiO_2 - TiO_2$ nanopillars can suppress the multipolar-mode resonances at non-resonant wavelengths, leading to highly saturated structural colors with a wide gamut. By independently and meticulously designing the periods and diameters along the x and y axes, the color palettes consisting of abundant dual colors can be obtained to meet the incident polarization angles. By performing PDN based on ResNets in deep learning to recognize extremely slight color variations, the colorimetric polarization-angle detection is realized in about 1 s with an accuracy of 99.4% within 0.7° error (100% within 1.4°) for the training dataset and 81.4% within 0.7° error (99.5% within 1.4° error) for the test dataset. Our approach can also be expanded to elliptically polarized incident light by using structural colors that respond to different elliptically polarized light, such as chiral structural colors that hold different near-field interferences or resonances for different polarizations. The generalization ability and prediction accuracy of the network can be further improved by increasing the amount of data in the training set and the depth of PDN. Our approach provides a new paradigm for polarization detection and can be potentially applied in various applications such as polarization encoded communications, fast diagnosis, and wearable intelligent devices.

Disclosures. The authors declare no conflicts of interest.

Data Availability. Data underlying the results may be obtained from the authors upon reasonable request.

[†]These authors contributed equally to this Letter.

REFERENCES

1. G. Kim, S. Cho, K. Chang, W. S. Kim, H. Kang, S.-P. Ryu, J. Myoung, J. Park, C. Park, and W. Shim, Adv. Mater. **29**, 1606120 (2017).
2. I. R. Howell, C. Li, N. S. Colella, K. Ito, and J. J. Watkins, ACS Appl. Mater. Interfaces **7**, 3641 (2015).
3. L. Xiao, A. Zhu, Q. Xu, Y. Chen, J. Xu, and J. Weng, ACS Appl. Mater. Interfaces **9**, 6931 (2017).
4. I. B. Burgess, N. Koay, K. P. Raymond, M. Kolle, M. LonÄar, and J. Aizenberg, ACS Nano **6**, 1427 (2012).
5. K. L. Naughton, L. Phan, E. M. Leung, R. Kautz, Q. Lin, Y. Van Dyke, B. Marmiroli, B. Sartori, A. Arvai, S. Li, M. E. Pique, M. Naeim, J. P. Kerr, M. J. Aquino, V. A. Roberts, E. D. Getzoff, C. Zhu, S. Bernstorff, and A. A. Gorodetsky, Adv. Mater. **28**, 8405 (2016).
6. T. H. Talukdar, B. Mccoy, S. K. Timmins, T. Khan, and J. D. Ryckman, Proc. Natl. Acad. Sci. USA **117**, 30107 (2020).
7. L. V. Poulikakos, M. Lawrence, D. R. Barton, S. S. Jeffrey, and J. A. Dionne, ACS Photon. **7**, 3216 (2020).
8. J. S. Lee, J. Y. Park, Y. H. Kim, S. Jeon, O. Ouellette, E. H. Sargent, D. H. Kim, and J. K. Hyun, Nat. Commun. **10**, 4782 (2019).
9. S. Sun, Z. Zhou, C. Zhang, Y. Gao, Z. Duan, S. Xiao, and Q. Song, ACS Nano **11**, 4445 (2017).
10. B. Yang, W. Liu, Z. Li, H. Cheng, D.-Y. Choi, S. Chen, and J. Tian, Nano Lett. **19**, 4221 (2019).
11. A. Kristensen, J. K. W. Yang, S. I. Bozhevolnyi, S. Link, P. Nordlander, N. J. Halas, and N. A. Mortensen, Nat. Rev. Mater. **2**, 16088 (2016).
12. K. Baek, Y. Kim, S. Mohd-Noor, and J. K. Hyun, ACS Appl. Mater. Interfaces **12**, 5300 (2020).
13. J.-R. Fan, J. Zhu, W.-G. Wu, and Y. Huang, Small **13**, 1601710 (2017).
14. S. Sun, W. Yang, C. Zhang, J. Jing, Y. Gao, X. Yu, Q. Song, and S. Xiao, ACS Nano **12**, 2151 (2018).
15. Y. Nagasaki, M. Suzuki, and J. Takahara, Nano Lett. **17**, 7500 (2017).
16. B. Yang, W. Liu, Z. Li, H. Cheng, S. Chen, and J. Tian, Adv. Opt. Mater. **6**, 1701009 (2018).
17. X. Zhang, S. Yang, W. Yue, Q. Xu, C. Tian, X. Zhang, E. Plum, S. Zhang, J. Han, and W. Zhang, Optica **6**, 1190 (2019).
18. P. C. Wu, W.-Y. Tsai, W. T. Chen, Y.-W. Huang, T.-Y. Chen, J.-W. Chen, C. Y. Liao, C. H. Chu, G. Sun, and D. P. Tsai, Nano Lett. **17**, 445 (2017).
19. G. Huang, Z. Liu, L. Maaten, and K. Q. Weinberger, in *IEEE Conference on Computer Vision and Pattern Recognition (CVPR)* (2017), p. 2261.
20. W. Liu, D. Ma, Z. Li, H. Cheng, D.-Y. Choi, J. Tian, and S. Chen, Optica **7**, 1706 (2020).
21. G. Hinton, L. Deng, D. Yu, G. E. Dahl, A. Mohamed, N. Jaitly, A. Senior, V. Vanhoucke, P. Nguyen, T. N. Sainath, and B. Kingsbury, IEEE Signal Process. Mag. **29**(6), 82 (2012).
22. D. Silver, A. Huang, C. J. Maddison, A. Guez, L. Sifre, G. Van Den Driessche, J. Schrittwieser, I. Antonoglou, V. Panneershelvam, M. Lanctot, S. Dieleman, D. Grewe, J. Nham, N. Kalchbrenner, I. Sutskever, T. Lillicrap, M. Leach, K. Kavukcuoglu, T. Graepel, and D. Hassabis, Nature **529**, 484 (2016).
23. W. Ma, F. Cheng, and Y. Liu, ACS Nano **12**, 6326 (2018).
24. Z. Liu, D. Zhu, S. P. Rodrigues, K.-T. Lee, and W. Cai, Nano Lett. **18**, 6570 (2018).
25. Z. Liu, S. Yan, H. Liu, and X. Chen, Phys. Rev. Lett. **123**, 183902 (2019).
26. Q. Zhang, C. Liu, X. Wan, L. Zhang, S. Liu, Y. Yang, and T. J. Cui, Adv. Theor. Simul. **2**, 1800132 (2019).
27. A. Krizhevsky, I. Sutskever, and G. E. Hinton, in *25th International Conference on Neural Information Processing Systems* (2012), Vol. **1**, p. 1097.
28. K. He, X. Zhang, S. Ren, and J. Sun, in *IEEE Conference on Computer Vision And Pattern Recognition (CVPR)* (2016), p. 770.